

Radio detections of two unusual cataclysmic variables in the VLA Sky Survey

M. E. Ridder,¹* C. O. Heinke,¹ G. R. Sivakoff,¹ & A. K. Hughes¹

¹ *University of Alberta, Physics Dept., CCIS 4-183, Edmonton, AB T6G 2E1, Canada*

Accepted XXX. Received YYY; in original form ZZZ

ABSTRACT

We report two new radio detections of cataclysmic variables (CVs), and place them in context with radio and X-ray detections of other CVs. We detected QS Vir, a low accretion-rate CV; V2400 Oph, a diskless intermediate polar (IP); and recovered the polar AM Her in the Very Large Array Sky Survey (VLASS) 2–4 GHz radio images. The radio luminosities of these systems are higher than typically expected from coronal emission from stars of similar spectral types, and neither system is expected to produce jets, leaving the origin of the radio emission a puzzle. The radio emission mechanism for these two CVs may be electron-cyclotron maser emission, synchrotron radiation, or a more exotic process. We compile published radio detections of CVs, and X-ray measurements of these CVs, to illustrate their locations in the radio - X-ray luminosity plane, a diagnostic tool often used for X-ray binaries, active galactic nuclei, and radio stars. Several radio-emitting CVs, including these two newly detected CVs, seem to lie near the principal radio/X-ray track followed by black hole X-ray binaries (BHXBs) at low luminosity, suggesting additional complexity in classifying unknown systems using their radio and X-ray luminosities alone.

Key words: cataclysmic variables — stars: dwarf novae — stars: individual: QS Vir — stars: individual: V2400 Oph — radio continuum: stars

1 INTRODUCTION

Cataclysmic variables (CVs) are binary systems in which a white dwarf (WD) accretes from an M or K type donor star (e.g., see review in Warner 2003). Accretion begins when the donor reaches the edge of its Roche lobe, but the accretion geometry is determined by the WD’s magnetic field. If the WD is weakly magnetic, then matter from the donor fills an accretion disk around the WD. These kinds of CVs periodically go into outburst (dwarf novae) caused by an increased accretion rate, or remain at a high accretion rate for long periods of time (novalikes). The moderately magnetic case (intermediate polars; IPs) results in a truncated accretion disk, where the inner region of the disk follows the field lines onto the poles. In the most extreme case (polars), there is no accretion disk and matter only flows along the WD’s magnetic field lines.

There are currently 33 known CVs detected in the radio at $\geq 3\sigma$ confidence and 16 marginal detections. Of these 33 CVs, 23 are magnetic (Barrett et al. 2020) and 10 are non-magnetic (Körding et al. 2008; Coppejans et al. 2015, 2016; Russell et al. 2016). The main hypotheses for the origin of radio emission from CVs are synchrotron emission from a jet (Russell et al. 2016; Mooley et al. 2017; Fender et al. 2019), or electron-cyclotron maser emission (ECME) near the WD or donor (Barrett et al. 2020). Even within a given class (e.g. novalike), there may be multiple processes responsible for the radio emission (Coppejans et al. 2015, 2016).

SS Cyg is a well-studied non-magnetic CV with a radio counterpart (Russell et al. 2016; Mooley et al. 2017; Fender et al. 2019). Multiple

radio flares coincide with its dwarf nova (DN) outbursts, and the evolution of the spectral index during one flare suggests a jet launched by the WD in SS Cyg (Fender et al. 2019). Unfortunately, there are not enough data for other DNe and novalikes to determine if their radio emission is also jet-powered (Coppejans et al. 2015, 2016). The prototypical polar, AM Her, is another well-known CV that has been observed at radio frequencies since the early 1980s (Chanmugam & Dulk 1982). The radio source in magnetic systems such as this has been suggested to be ECME, which is the result of a plasma instability (Barrett et al. 2020). In the weakly relativistic regime, ECME produces narrow band, highly circularly polarized emission. In order to produce the instability, the plasma environment needs to be low-density ($n < 10^{-12} \text{ cm}^{-3}$; Barrett et al. 2020) and highly magnetized, which is the case in the corona of the donor star or near the WD, possibly adjacent to the accretion column.

Among the other radio bright binaries containing white dwarfs are AR Sco (Marsh et al. 2016) and AE Aqr (Bookbinder & Lamb 1987). These are CV-like with a M-K type secondary and WD primary, but unlike CVs, there is little or no accretion, and the observed electromagnetic radiation is thought to be produced by more complex processes. AR Sco is commonly referred to as a white dwarf pulsar, as its WD’s magnetic poles sweep over the companion with a period of 1.95 minutes, which produces emission at the WD spin period and the beat period between the spin and orbital periods (Marsh et al. 2016; Buckley et al. 2017; Marcote et al. 2017; Garnavich et al. 2019). The leading explanation for AR Sco’s emission mechanism, based on the high luminosity of the system (larger than either star should be), the beat-period signal (suggesting reprocessing of radiation from the WD striking the companion), and the rapid spindown of the WD

* E-mail: mridder@ualberta.ca

(indicating a high B field of 100–500 MG, Buckley et al. 2017), is that the emission is largely synchrotron radiation from electrons accelerated by the WD magnetic field and/or interaction between the WD and companion magnetic fields (e.g. Marsh et al. 2016; Takata et al. 2018).

AE Aqr is a propeller system, meaning that as material from the donor falls towards the WD, it is flung out of the system by the magnetic field of the rapidly spinning WD (Eracleous & Horne 1996; Wynn et al. 1997), with radio emission thought to be produced by acceleration of electrons in the outflowing material in shocks (Bastian et al. 1988; Meintjes & Venter 2003). The only known AE Aqr twin is LAMOST J024048.51+195226.9 (hereafter J0240, Thorstensen 2020; Garnavich et al. 2021; Pretorius et al. 2021; Pelisoli et al. 2022). Since we do not yet know the exact process that produces radio emission in CVs, we include AE Aqr, LAMOST J0240, and AR Sco in our plots as references.

In this paper we discuss two new detections of unusual CVs in Epochs 1 and 2 of the Very Large Array Sky Survey (VLASS), QS Vir and V2400 Oph. QS Vir is a low accretion-rate ($\dot{M} = 1.7 \times 10^{-13} M_{\odot} \text{ yr}^{-1}$), eclipsing CV, sometimes referred to as a pre-CV (O’Donoghue et al. 2003; Matraga et al. 2012). V2400 Oph is a diskless IP that may undergo diamagnetic blob accretion, in which blobs of matter from the donor star orbit the WD and eventually accrete or transfer back to the donor (Langford et al. 2022). Based on the VLASS data, V2400 Oph has shown the brightest radio emission of any CV to date.

In Section 2 we discuss the archival radio observations of QS Vir and V2400 Oph. In Section 3 we explain the analysis of these radio images as well as archival X-ray data. In Section 4 we discuss the implications of our results. Throughout this paper, we quote errors at $1\text{-}\sigma$ unless otherwise noted.

2 VLASS OBSERVATIONS

The Very Large Array Sky Survey (VLASS; Lacy et al. 2020) is conducted using the VLA S band (2–4 GHz) in a raster scan, with about 4.5 seconds exposure time on any source in each epoch, assuming a scan speed of $3.31''/\text{s}$ and a prime beam of $45/\nu_{\text{GHz}}$. Upon completion, the full sky (above -40 declination) will be visited three times by VLASS; at the time of writing, both the first and second epochs of observations of the sky above -40 degrees declination are now available. Rapid CLEAN processing by NRAO produces Quick-Look images, which have a typical noise of $120 \mu\text{Jy}$ (Gordon et al. 2021). Using the Canadian Initiative for Radio Astronomy Data Analysis¹ (CIRADA) image cutout service, an online tool that generates cutout images of radio and IR surveys, we retrieved images of each object from the list of 1681 CVs and related systems in Ritter & Kolb (2003), which were crossmatched with *Gaia* EDR3 (Gaia Collaboration et al. 2021). We queried all VLASS epochs in late 2021 when observations up to Epoch 2.1 were available. We identified three radio counterparts; the polar AM Her (previously known to be radio-emitting, Chanmugam & Dulk 1982), QS Vir, and V2400 Oph. When Epoch 2.2 was released, we checked for new observations of these three CVs, and when astrometric corrections were provided for Epoch 1, we updated our data. After astrometric corrections are applied, the absolute astrometric systematic uncertainty is $\sim 0.25''$ (Lacy 2021), which is better than that discussed in Gordon et al. (2020).

The radio images of QS Vir, V2400 Oph, and AM Her are shown in

Figures 1, 2, and 3. Both QS Vir and V2400 Oph were detected only in the first epoch, while AM Her was detected in both epochs. As our search was performed only on the Epochs 1.1 – 2.1, and both QS Vir and V2400 Oph appear to be transient in the radio, it seems plausible that additional CVs, including those in Ritter & Kolb (2003), may be detected in the second and third epochs of VLASS.

Based on visual inspections of the images, we do not believe the sources are likely to arise from image artifacts. We obtained source positions and fluxes with Common Astronomy Software Applications (CASA) 6.5 (McMullin et al. 2007), software written by the National Radio Astronomy Observatory (NRAO) for analyzing radio data. The `imfit` algorithm fits a two-dimensional Gaussian distribution to a source inside a given position and radius, then returns a source position, flux, and flux error. To obtain the position error, we calculated the width of the beam in RA and declination. Since the synthesized beam is reported in units of the full-width-half-maximum, we divided the projected beam sizes by $2 \times \text{SNR}$ to determine the statistical error in centroiding. Because there is a systematic error of 1/10 of the beam in VLASS, we added this term to the last in quadrature to find the total error. We found the position of the source in Figure 1a is $0.4''$ away from the coordinates for QS Vir in *Gaia* EDR3. For Figure 2a, the source is $0.7''$ away from the *Gaia* EDR3 position of V2400 Oph. The radio source near AM Her is offset by $0.2''$ (Figure 3a) and $0.1''$ (Figure 3b), in the two epochs respectively. The positions of the radio counterparts in these images are consistent within 2σ of the *Gaia* EDR3 coordinates of each object.

With the `imfit` algorithm described above, we centered a region on each source’s *Gaia* position and fixed all Gaussian components to the shape of the synthesized beam for the fit. We characterized the background with the function `imstat` and estimated the noise from the root-mean-square statistic in an annulus around each source. The measured fluxes of QS Vir and V2400 Oph can be found in Table 2. Each CV is detected at least once at $>5\sigma$.

3 ANALYSIS

3.1 Chance coincidence?

To calculate the likelihood that our radio detections are simply spurious detections of background AGN, we first need to estimate the density of background AGN. We take two approaches to this. First, we find the number of radio sources in the vicinity of QS Vir and V2400 Oph, using VLASS. Using the VLASS catalog of source from Gordon et al. (2020), there are 179 and 133 reliable components (`Duplicate_flag < 2` and `Quality_flag == 0`) from Gordon et al. (2020) within a 1 degree radius around QS Vir and V2400 Oph, respectively. We thus derive an average background source density of 3.8×10^{-6} sources per square arcsecond.

We searched for VLASS emission near the 1681 objects from the Ritter & Kolb (2003) catalog that also had *Gaia* EDR3 positions. Given typical astrometric errors in $5\text{-}\sigma$ detected VLASS sources of $0.35''$, we consider matches out to 3σ , or $1.05''$. Given the 1681 potential objects, we estimate the probability of a chance coincidence at 0.022.

Since we were able to search for radio sources fainter than included in the (conservative) catalog of Gordon et al. (2020), this chance coincidence calculation may be an underestimate. A more conservative estimate uses the expected total VLASS source number of 5.3 million anticipated detections (Lacy et al. 2020), divided by the 33885 square degrees to be surveyed. Since this number is for the stacked combination of all three epochs, we use Owen & Morrison

¹ <https://cirada.ca/>

Table 1. Coordinates of our detected sources, from *Gaia* EDR3 and in VLASS, and *Gaia* distances (Baileer-Jones et al. 2021). The errors quoted on VLASS distances are 1-sigma. Offsets are rounded to the nearest 0.05".

Name	<i>Gaia</i> RA (deg)	<i>Gaia</i> Dec (deg)	VLASS RA (deg)	VLASS Dec (deg)	Offset (arcsec)	Distance (pc)
QS Vir	207.466870	-13.226865	207.46694(9)	-13.22678(11)	0.40	50.1 ^{+0.07} _{-0.06}
V2400 Oph	258.151755	-24.245759	258.15156(8)	-24.24585(8)	0.75	700 ⁺¹⁰ ₋₁₁
AM Her (1.1)	274.054911	49.868113	274.05489(11)	49.86816(9)	0.20	87.9±0.2
AM Her (2.1)	274.054911	49.868113	274.05496(10)	49.86810(9)	0.10	87.9±0.2

Table 2. VLASS flux measurements (2 – 4 GHz) of all sources when they were observed. The value for QS Vir in Epoch 2.2 and V2400 Oph in Epoch 2.1 are three sigma upper limits.

Name	Flux (μ Jy)	Epoch	Observation date
QS Vir	970±160	1.2	2019 April 25
QS Vir	≤ 510	2.2	2022 January 31
V2400 Oph	640±120	1.1	2018 February 5
V2400 Oph	≤ 620	2.1	2020 October 23
AM Her	640±120	1.1	2017 September 9
AM Her	880±150	2.1	2020 August 11

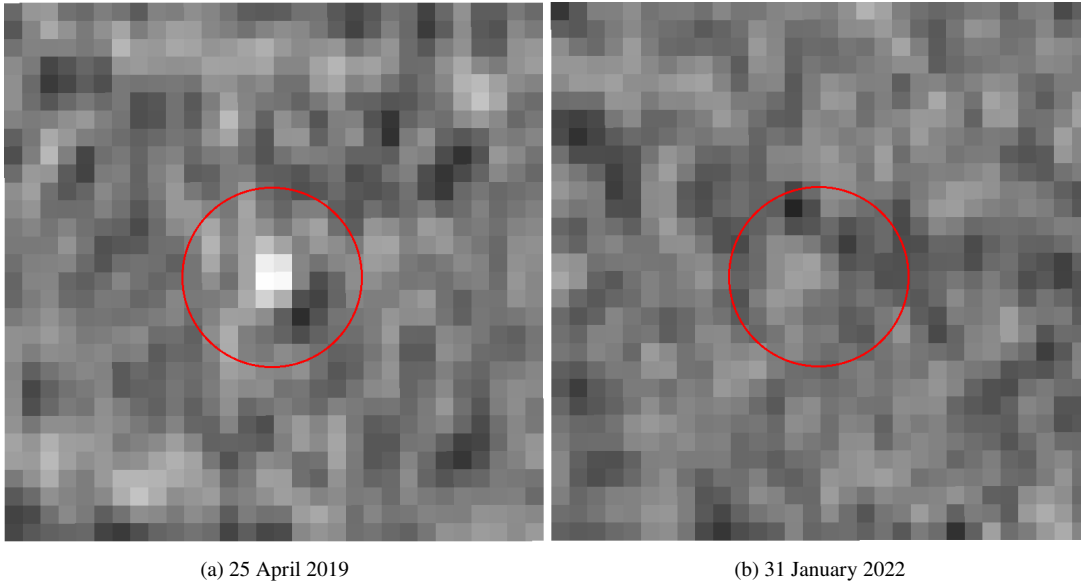


Figure 1. VLASS-QL cutouts of QS Vir on 2019 April 25 and 2022 January 31. The images are 30''×30'' and the red circles have a 5 arcsecond radius, centered on QS Vir's *Gaia* coordinates.

(2008) to estimate that there will be about 2.3 million anticipated detections in a single VLASS Epoch, and estimate that the background source density should be about 5.2×10^{-6} sources per square arcsecond. Given the 1681 error circles searched, we estimate the probability of a chance coincidence at 0.029.

We conclude that it is unlikely that either of our newly detected radio sources are chance coincidences, and that we have detected radio counterparts to QS Vir and V2400 Oph.

3.2 X-ray flux measurements

Comparison of X-ray and radio luminosities can be helpful in understanding accretion behaviour. Although we did not have (near)-simultaneous X-ray observations, non-simultaneous X-ray observations can still be useful, especially if the X-ray flux is not known to

vary by orders of magnitude. Polars, for instance, appear to be only moderately variable, except for their drops into "low states" with little accretion, which appear to occur about half the time (Ramsay et al. 2004b). AM Her, for example, shows variability of about an order of magnitude between the Second *ROSAT* All-Sky Survey Source Catalog (2RXS; Boller et al. 2016) and the *XMM-Newton* Serendipitous Source Catalog (4XMM-DR11; Webb et al. 2020), $\sim 10^{-13}$ and $\sim 10^{-12}$ erg s⁻¹ cm⁻² respectively, from 0.5 - 1 keV. However, there is more uncertainty in DNe because of the X-ray flux's dependence on whether the object is in outburst or quiescence. While the radio observations of the DNe in our dataset were taken during outburst (Coppejans et al. 2016), we cannot be certain whether the same is true for X-ray catalog data. Similarly, we cannot determine what accretion state the polars in our dataset were in during the X-ray or radio observations. We estimate the X-ray variability of our

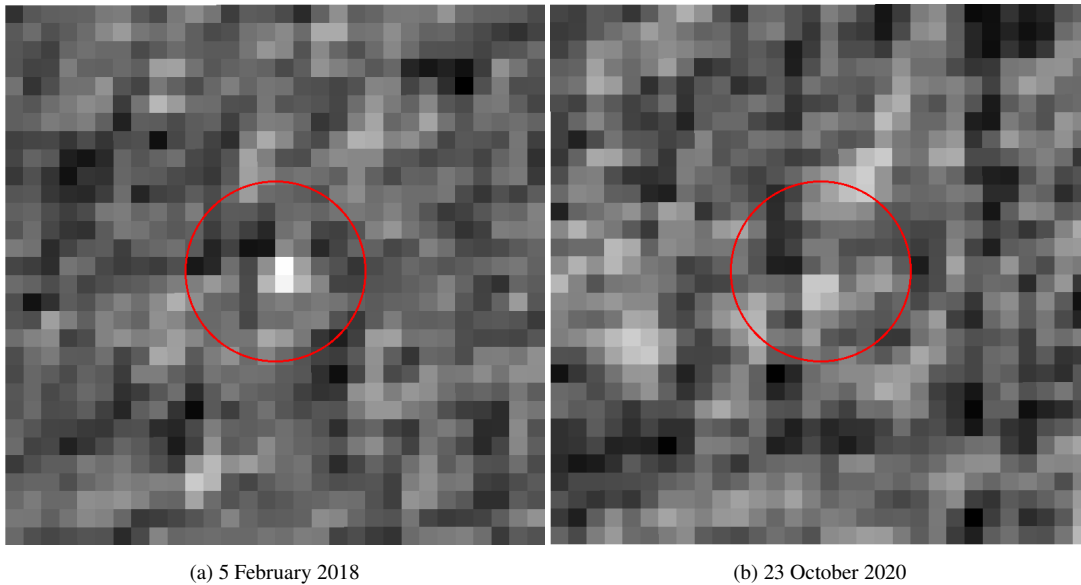


Figure 2. VLASS-QL cutouts of V2400 Oph on 2018 February 5 and 2020 October 23. The images are $30'' \times 30''$ and the red circles have a $5''$ radius, centered on V2400 Oph’s *Gaia* coordinates.

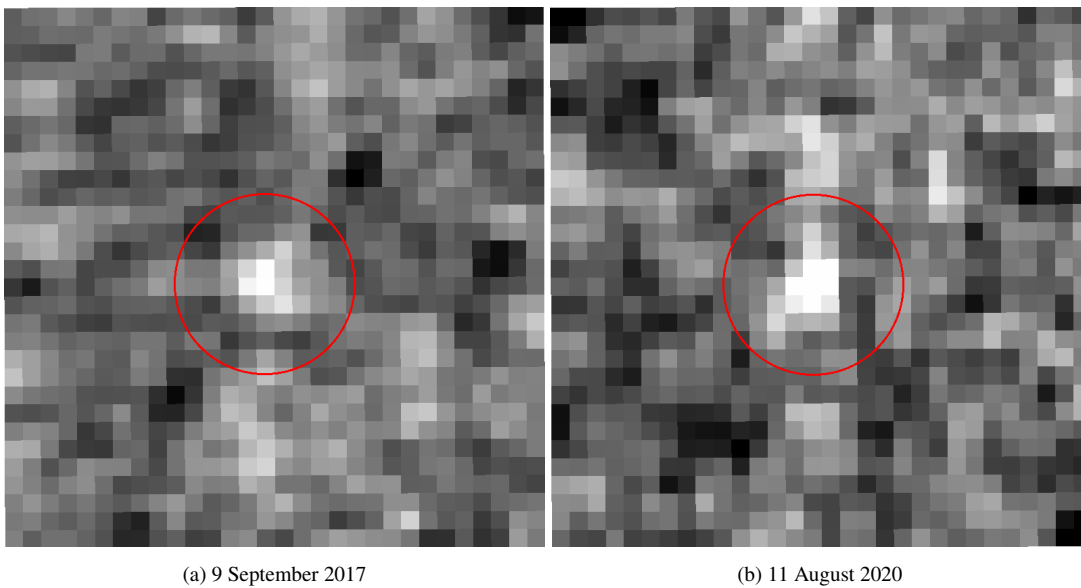


Figure 3. VLASS-QL cutouts of AM Her on 2017 September 9 and 2020 August 11. The images are $30'' \times 30''$ and the red circles have a 5 arcsecond radius, centered on AM Her’s *Gaia* coordinates.

sources by comparing their detections in the improved *Swift* XRT Point Source Catalog (2SXPS; Evans et al. 2020) and 2RXS (Figure 4), which allows us to estimate a dispersion of $\sim 3 \text{ ct s}^{-1}$ between multiple X-ray observations of the same source.

To obtain catalog X-ray data, we queried the HEASARC database using the *Gaia* EDR3 coordinates of QS Vir and V2400 Oph, which returned detections in 4XMM-DR11. To compare to other radio-detected CVs (Coppejans et al. 2015, 2016; Barrett et al. 2020), we retrieved (generally non-simultaneous) X-ray data from their positions. These objects were observed in 4XMM-DR11, 2SXPS, the *ROSAT* All-Sky Survey Bright Source Catalog (RASS-BSC; Voges et al. 1999), and 2RXS. Only SS Cyg has published simultaneous X-ray and radio light curves during outbursts, for which we chose to

plot points at the highest radio flux and the highest X-ray count rate from Russell et al. (2016). To obtain the exact *Swift* flux, we fit SS Cyg’s spectra using the fitting tool provided by the UK Swift Science Data Centre² (Evans et al. 2009).

To convert count rates from these catalogs into luminosities, we searched the literature for spectral fits of magnetic CVs and non-magnetic CVs. For the few that had a spectral fit, we used the reported model and absorption column density N_H to obtain the unabsorbed flux with CXC PIMMS³. When only catalog data were available, we

² https://www.swift.ac.uk/user_objects/

³ <https://cxc.harvard.edu/toolkit/pimms.jsp>

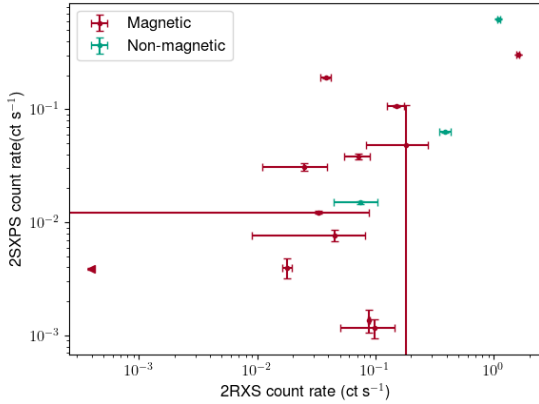


Figure 4. ROSAT (2RXS) vs. Swift (2SXPS) count rates of the objects in Tables 3 and 4. We find a typical scatter in X-ray count rates of $\sigma_X \sim 3 \text{ ct s}^{-1}$.

used CXC Colden⁴ to estimate N_H provided by Dickey & Lockman (1990). For magnetic CVs, we followed the convention in Ramsay et al. (1994), choosing a thermal bremsstrahlung model with a 30 keV temperature for energies greater than 0.5 keV and a blackbody model with a 30 eV temperature for energies between 0.1 and 0.4 keV. In order to do this when RASS-BSC or 2RXS data were available, we used the hardness ratio between the two bands 0.1–0.4 keV and 0.5–2 keV to estimate the count rates in both. When 2SXPS data was available we used the hardness ratio between the bands 0.3–1 keV and 1–2 keV to determine whether there was a significant soft component and if so, applied a blackbody model to the 0.3–1 keV count rate. If not, a thermal bremsstrahlung model was used for that energy range. Above 1 keV, we assumed the bremsstrahlung model would dominate in all cases.

Of the novalikes in Coppejans et al. (2015) and Hewitt et al. (2020), only TT Ari had an X-ray spectral fit (Mauche & Mukai 2002). Thus we assumed the other novalikes should be fit with a similar model and characteristic temperature; we assumed a single MEKAL model with an average temperature of 7 keV. Of the dwarf novae in Coppejans et al. (2016), only Z Cam (Saitou et al. 2012) and SU UMa (Collins & Wheatley 2010) had X-ray spectral fits that could be converted with PIMMS. For these, we assumed a MEKAL model (as used in both of the fits) and an average characteristic temperature of 11 keV.

When fluxes were available in 4XMM-DR11, we made an approximate conversion to 1–10 keV by taking the full band (Band 8, 0.2–12 keV) and subtracting two soft bands (Band 1, 0.2–0.5 keV; Band 2, 0.5–1 keV). Assuming very few photons were detected between 10 and 12 keV, the full band from 4XMM-DR11 approximates the 0.1–10 keV flux.

For data from a single band in RASS-BSC and 2RXS, we use the error given in each catalog. For data from 4XMM-DR11, we assumed the largest error quoted for the full band would be roughly the same as that for 1–10 keV. Some of the errors on *Swift*'s 2–10 keV and 0.3–1 keV bands were of the same magnitude so these were added in quadrature.

⁴ <https://cxc.harvard.edu/toolkit/colden.jsr>

3.3 Radio - X-ray luminosity plane

We compare the radio and X-ray luminosities of the CVs, extracted from the literature as above, in Figure 5. The data points here are also shown in Tables 3 and 4. We assumed a flat spectrum up to 5 GHz, thus multiplying the flux density by $(5 \times 10^9 \text{ Hz} \times 4\pi d^2)$ to infer a radio luminosity. While some CVs have been detected at higher frequencies than 5 GHz (e.g. EQ Cet at 18–26.5 GHz), we do not have clear measurements of the shapes of CV spectra. Using a flat spectrum up to 5 GHz (while logically inconsistent for CVs detected at higher frequencies) has the benefit of allowing comparison between CVs (assuming they all have the same spectrum), and with the literature, both of CVs and X-ray binaries (e.g. Bahramian et al. 2018). We have also plotted the well-known relationship between the X-ray and radio luminosity of BHXBs (Gallo et al. 2003, black dotted line in Figure 5 of this paper). Included in this figure are our detections, previously known radio CVs, and the unique systems, AR Sco and AE Aqr. V2400 Oph stands out in the upper right corner, far brighter in radio and X-ray than most magnetic and non-magnetic CVs. The second brightest CV in the radio is V1323 Her, another IP (Barrett et al. 2020). QS Vir is near the bottom left, near several magnetic CVs. For comparison of our data to X-ray binaries, we have plotted a transitional millisecond pulsar (tMSP; PSR J1023+0038; Bahramian et al. 2018; Deller et al. 2015; Bogdanov 2018) and three BHXBs (A0620-00, XTE J1118+480, Cen X-4; Bahramian et al. 2018; Fender et al. 2010; Gallo et al. 2014; Tudor et al. 2017).

Sources in Barrett et al. (2020) with radio detections below $3\text{-}\sigma$ (Cas 1, FL Cet, Hya 1, HS0922+1333, and Her 1) were excluded in this plot. We plotted the highest and lowest radio fluxes, for objects with multiple radio detections, as a range denoted with a dashed line.

3.4 Radio luminosity and orbital period

Figure 7 shows our detections compared to previously known radio CVs, AR Sco, AE Aqr, and the candidate propeller system LAMOST J0240 (note that the latter is not yet X-ray-detected, and thus not shown in Figure 5). V2400 Oph's orbital period is much shorter than the propellers, but it is similarly bright, as is the other IP, V1323 Her. QS Vir is within the cluster of magnetic and non-magnetic CVs, including AM Her.

4 DISCUSSION

The proximity of our detections and the rest of the CV population to the hard-state BH X-ray binary relationship in Figure 5 suggests a possible problem for radio/X-ray identification of quiescent BHXBs. The radio-X-ray relation has often been used to suggest that a given radio source near the BHXB line is likely to be a BHXB (e.g. Bahramian et al. 2020; Zhao et al. 2020; Shishkovsky et al. 2018). However, our results show that there could be significant CV contamination among sources near this line. We note that CVs often show substantial X-ray variability of an order of magnitude or more, and, based on the limited observations so far, radio variability seems common at well. Simultaneous X-ray and radio observations would be very useful. We provide a series of radio observations of AM Her in Figure 8 to illustrate the observed variability on a timescale of years. Except for a flare of $9.7 \pm 2.3 \text{ mJy}$ (Dulk et al. 1983) and a $100 \mu\text{Jy}$ upper limit detected by Bastian et al. (1985), the flux varies between ~ 200 to $\sim 700 \mu\text{Jy}$. However, as most of our data is non-simultaneous, interpreting Figure 5 should be done with caution.

Given the limited VLASS data at present, we cannot be certain

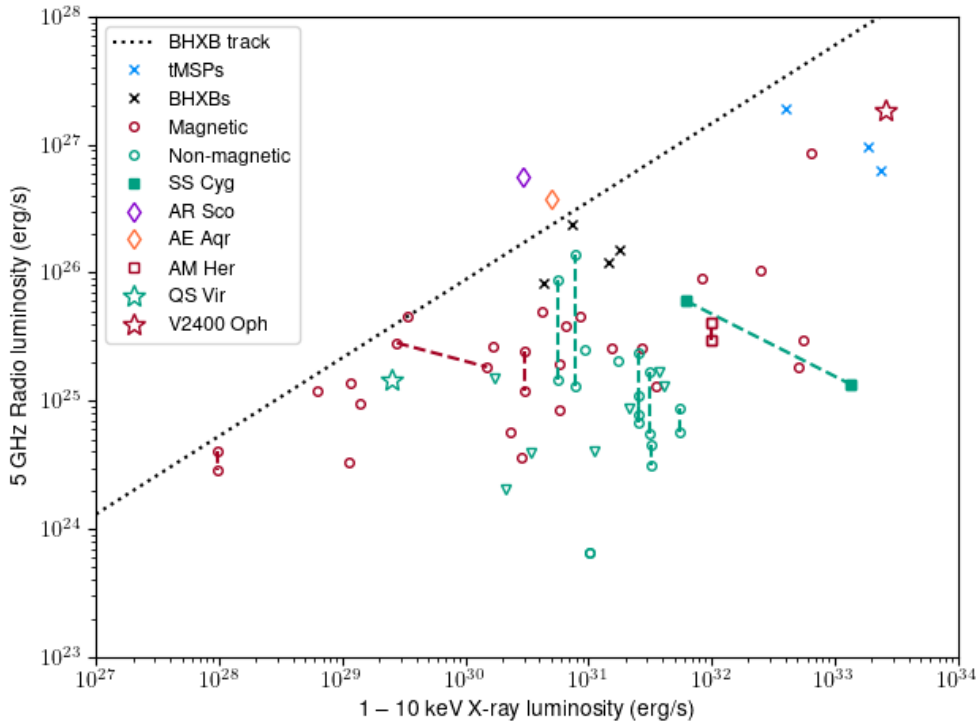


Figure 5. X-ray vs. radio luminosities of CVs (and related systems) with detections in both bands. Two locations of simultaneous data (filled symbols) are plotted for SS Cyg, one at maximum X-ray luminosity and one at maximum radio luminosity (Russell et al. 2016). All other data are non-simultaneous (open symbols). Multiple radio detections of the same object at different luminosities are connected with dashed lines. The black dotted line marks the L_X - L_R relationship for BHXBs (Gallo et al. 2003).

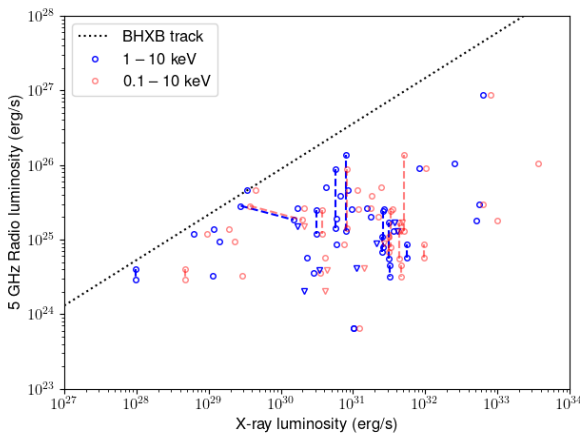


Figure 6. Comparing the effects of using the 1–10 keV X-ray luminosity vs. the 0.1–10 keV X-ray luminosity for the positions of radio-detected CVs in the radio/X-ray plane. The black dotted line marks the L_X - L_R relationship for BHXBs (Gallo et al. 2003).

of the emission mechanism behind the radio counterparts of V2400 Oph and QS Vir. In the case of QS Vir, the extremely low accretion rate paired with the known lack of an accretion disc suggests radio emission originates in ECME rather than jets. Radio flares on isolated M dwarfs are fairly common, and Hallinan et al. (2008) propose that the dominant radio emission mechanism in late type dwarfs is ECME. QS Vir has displayed coronal flares from its M-type donor star in the past (O’Donoghue et al. 2003), suggesting the radio flares could be

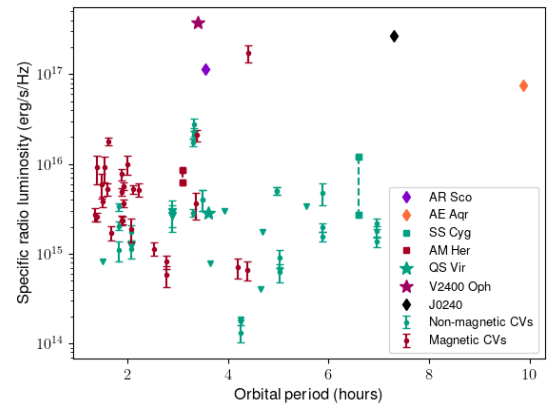


Figure 7. The orbital period in hours for our sample vs. specific radio luminosity. Here we plot each individual observation of magnetic and non-magnetic CVs in Barrett et al. (2020); Coppejans et al. (2015, 2016); Hewitt et al. (2020), unlike Figure 5. LAMOST J0240 is an AE Aqr twin that we do not show in Figure 5 since it currently is undetected in X-rays.

from the donor. However, Güdel (2002) shows that M and K dwarf radio detections in the cm band generally reach 10^{15} erg/s/Hz at most, which for 5 GHz gives a maximum $L_R = 5 \times 10^{23}$ erg/s; a factor of 20 below QS Vir’s detection. This does not prove that the radio emission cannot come from the donor star, as there is a candidate detection of brighter radio emission from a young M-type brown dwarf (2MASS J16044075–1936525) in Ling et al. (2022), at $L_R(5 \text{ GHz}) = 1.1 \times 10^{27}$

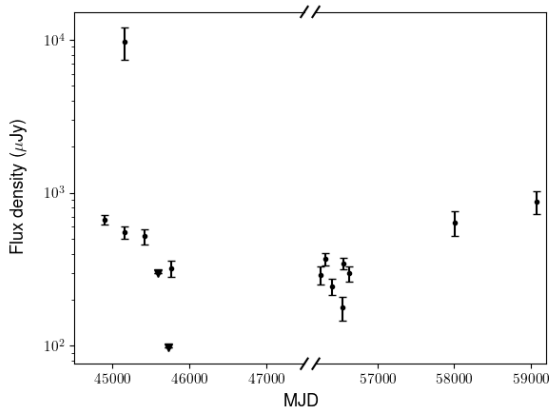


Figure 8. 4.9 GHz radio observations of AM Her from 1981 to 2013 (MJD 44900 – 56600) (Dulk et al. 1983; Bastian et al. 1985; Gawroński et al. 2018) and the 2 – 4 GHz VLASS observations from 2017 and 2020 (MJD 58000 – 59100). Upper limits are at the $1-\sigma$ level. For the majority of its history, the radio flux varies by a factor of ~ 4 ; the outlying points are the 9.7 ± 2.3 mJy flare and lower limit of $100 \mu\text{Jy}$.

erg/s. However, such radio emission is quite rare; Ling et al. (2022) surveyed 2600 (mostly young) stellar objects and detected only 6 of them in radio. Ling et al. (2022) produced a stacked 5 GHz radio luminosity upper limit of $< 1.3 \times 10^{23}$ erg/s for the RECONS sample (821 M stars within ~ 70 pc from Earth, Henry et al. 2018). Similarly, Launhardt et al. (2022) observed 170 young stars at 6 GHz, finding a half dozen detections near 10^8 W/Hz, or $L_R(5 \text{ GHz}) = 5 \times 10^{24}$ erg/s, but only one subgiant (V875 Per) brighter than QS Vir.

The source of the radio emission in V2400 Oph is even more difficult to explain. Its larger (by a factor of 100) radio luminosity (larger than any known M or K dwarf) would make ECME from the companion very surprising, while the lack of an accretion disc in the system makes the jet hypothesis unlikely. Langford et al. (2022) suggest that the accretion flow in V2400 Oph consists of a series of disconnected diamagnetic blobs (King 1993; Littlefield et al. 2021), which may either ride down the magnetic field lines to the magnetic poles of the white dwarf (generating the clearly observed spin periodicity), or gain energy from the magnetic field and be expelled, likely back to the donor star. This suggests the possibility of a similarity in the radio emission mechanism between V2400 Oph and the propeller systems AE Aquarii and J0240, which also expel material and have similar radio luminosity to V2400 Oph. On the other hand, V2400 Oph has not shown evidence for ~ 3000 km/s motion of propeller-launched blobs, as seen in AE Aquarii and J0240. Alternatively, Kennedy et al. (2020) identify evidence of high-velocity (600–1000 km/s) features during a low state of the IP FO Aquarii, which they suggest may be attributed to a jet or fast outflow. IPs lack a disk near the WD surface, which makes the formation of a jet in such systems challenging to justify theoretically. If this is indeed ECME, the source could be akin to the model for polars in Barrett et al. (2020), near the short-lived accretion stream caused by the blobs.

Future work on these CVs will include longer radio observations of these systems to measure the spectral index, polarization, and (with simultaneous X-ray observations) place the system firmly on the L_x/L_r plot. We do not know if there is a pattern to the radio flares, nor how frequently they recur, so a series of several 1-hour observations on different days may be the best option to catch their radio emission and advance our understanding of these unusual systems.

ACKNOWLEDGEMENTS

COH is supported by NSERC Discovery Grant RGPIN-2016-04602. GRS and AJH are supported by NSERC Discovery Grant RGPIN-2021-04001. The National Radio Astronomy Observatory is a facility of the National Science Foundation operated under cooperative agreement by Associated Universities, Inc. This research has made use of the CIRADA cutout service at URL cutouts.cirada.ca, operated by the Canadian Initiative for Radio Astronomy Data Analysis (CIRADA). CIRADA is funded by a grant from the Canada Foundation for Innovation 2017 Innovation Fund (Project 35999), as well as by the Provinces of Ontario, British Columbia, Alberta, Manitoba and Quebec, in collaboration with the National Research Council of Canada, the US National Radio Astronomy Observatory and Australia’s Commonwealth Scientific and Industrial Research Organisation. This research also made use of TOPCAT (Taylor 2005), software designed to handle large astronomical datasets with virtual observatory tools.

DATA AVAILABILITY

VLASS Quicklook data, including those used for this paper, are available via <https://cirada.ca/vlasscatalogueq10>.

REFERENCES

- Abada-Simon M., Lecacheux A., Bastian T. S., Bookbinder J. A., Dulk G. A., 1993, *ApJ*, **406**, 692
- Bahramian A., et al., 2018, Radio/X-ray correlation database for X-ray binaries, doi:10.5281/zenodo.1252036, <https://doi.org/10.5281/zenodo.1252036>
- Bahramian A., et al., 2020, *ApJ*, **901**, 57
- Bailer-Jones C. A. L., Rybizki J., Founesneau M., Demleitner M., Andrae R., 2021, *AJ*, **161**, 147
- Barrett P., Dieck C., Beasley A. J., Mason P. A., Singh K. P., 2020, *Adv. in Space Res.*, **66**, 1226
- Bastian T. S., Dulk G. A., Chanmugam G., 1985, in Hjellming R. M., Gibson D. M., eds, *Astrophysics and Space Science Library* Vol. 116, Radio Stars, pp 225–228, doi:10.1007/978-94-009-5420-5_30
- Bastian T. S., Dulk G. A., Chanmugam G., 1988, *ApJ*, **324**, 431
- Bogdanov S., 2018, X-rays from Radio Millisecond Pulsars (arXiv:1711.04791), doi:10.1017/S1743921317011553
- Boller T., Freyberg M. J., Trümper J., Haberl F., Voges W., Nandra K., 2016, *A&A*, **588**, A103
- Bonnet-Bidaud J. M., et al., 2020, *A&A*, **633**, A145
- Bookbinder J. A., Lamb D. Q., 1987, *ApJ*, **323**, L131
- Buckley D. A. H., Meintjes P. J., Potter S. B., Marsh T. R., Gänsicke B. T., 2017, *Nature Astronomy*, **1**, 0029
- Chanmugam G., Dulk G. A., 1982, *ApJ*, **255**, L107
- Collins D. J., Wheatley P. J., 2010, *MNRAS*, **402**, 1816
- Coppejans D. L., Körding E. G., Miller-Jones J. C. A., Rupen M. P., Knigge C., Sivakoff G. R., Groot P. J., 2015, *MNRAS*, **451**, 3801
- Coppejans D. L., et al., 2016, *MNRAS*, **463**, 2229
- Deller A. T., et al., 2015, *ApJ*, **809**, 13
- Dickey J. M., Lockman F. J., 1990, *ARA&A*, **28**, 215
- Dulk G. A., Bastian T. S., Chanmugam G., 1983, *ApJ*, **273**, 249
- Eracleous M., Horne K., 1996, *ApJ*, **471**, 427
- Eracleous M., Halpern J., Patterson J., 1991, *ApJ*, **382**, 290
- Evans P. A., et al., 2009, *MNRAS*, **397**, 1177
- Evans P. A., et al., 2020, *ApJS*, **247**, 54
- Fender R. P., Gallo E., Russell D., 2010, *MNRAS*, **406**, 1425
- Fender R., Bright J., Mooley K., Miller-Jones J., 2019, *MNRAS*, **490**, L76
- Gaia Collaboration et al., 2021, *A&A*, **649**, A1
- Gallo E., Fender R. P., Pooley G. G., 2003, *MNRAS*, **344**, 60

Table 3. The fluxes for magnetic CVs used to generate Figure 5 and 6, including AR Sco, AE Aqr, AM Her, and V2400 Oph. Refer to Table 4 for non-magnetic CVs.

Name	RA (deg)	Dec (deg)	Distance (pc)	1–10 keV flux (erg s ⁻¹ cm ⁻²)	0.1–10 keV flux (erg s ⁻¹ cm ⁻²)	Radio band (GHz)	Radio flux (μJy)	X-ray ref.	Radio ref.
EQ Cet	22.21913	-23.66237	283 ⁺⁵ ₋₈	9±4 × 10 ⁻¹³	1.2±0.4 × 10 ⁻¹²	18 – 26.5	96±30	9	2
BS Tri	32.37423	28.54133	277 ⁺⁸ ₋₇	1.7±0.6 × 10 ⁻¹²	1.9±0.6 × 10 ⁻¹²	8 – 12	57±9	22	2
EF Eri	48.5543	-22.5948	163 ⁺⁶⁶ ₋₅₀	3.7×10 ⁻¹⁴	6.0×10 ⁻¹⁴	8 – 12	87±15	19	2
UZ For	53.86947	-25.73939	238 ±3	2.5±0.7 × 10 ⁻¹³	3.1±0.7 × 10 ⁻¹³	4 – 8	78±9	20	2
RXJ0502.8+1624	75.71247	16.40595	217 ⁺¹³ ₋₁₀	1.0±0.2 × 10 ⁻¹⁰	1.1±0.2 × 10 ⁻¹⁰	8 – 12	105±32	3	2
LW Cam	106.04185	62.05777	549 ±19	2.3±0.5 × 10 ⁻¹²	2.8±0.5 × 10 ⁻¹²	8 – 12	50±5*	22	2
VV Pup	123.77841	-19.05524	135.3 ±0.7	2.7×10 ⁻¹²	3.5×10 ⁻¹²	8 – 12	79±14	4	2
FR Lyn	133.55839	39.09354	480 ⁺⁵⁰ ₋₄₀	2.4±1.1 × 10 ⁻¹³	6.5±1.1 × 10 ⁻¹³	8 – 12	28±4	22	2
WX LMi	156.61466	38.75055	96.8 ⁺⁴⁰ _{-0.6}	8.7×10 ⁻¹⁵	4.2×10 ⁻¹⁴	4 – 8	73±12	23	2
...	8 – 12	52±14
ST LMi	166.41570	25.10783	114.2 ±0.9	4.0±0.5 × 10 ⁻¹⁴	6.0±0.6 × 10 ⁻¹⁴ *	8 – 12	153±15*	24	2
AR UMa	168.93529	42.97289	98.6 ±0.5	2.4 × 10 ⁻¹³	3.2 × 10 ⁻¹³	4 – 8	489±49*	21	2
...	1.3 × 10 ⁻¹²	1.7 × 10 ⁻¹²	18 – 26.5	317±32*
EU UMa	177.48200	28.75199	287 ⁺¹⁶ ₋₁₅	6 ⁺² ₋₅ × 10 ⁻¹³	...	8 – 12	39±5	14	2
V1043 Cen	198.32121	-32.98694	172.9 ±0.9	7.9±0.8 × 10 ⁻¹³ *	1.0±0.1 × 10 ⁻¹² *	8 – 12	20±5	24	2
J1503-2207	225.97494	-22.11956	387±18	1.5±0.2 × 10 ⁻¹²	2.0±0.2 × 10 ⁻¹²	8 – 12	29±5	9	2
BM CrB	235.26945	36.04798	423 ⁺¹⁴ ₋₁₆	1.6±1.5 × 10 ⁻¹⁴	2.1±1.5 × 10 ⁻¹⁴	8 – 12	43±15	24	2
MR Ser	238.19645	18.94162	131.2 ^{+0.5} _{-0.7}	1.5 × 10 ⁻¹²	1.8 × 10 ⁻¹²	4 – 8	239±24*	13	2
...	8 – 12	116 ±15
MQ Dra	238.37941	55.27067	180.7 ^{+2.1} _{-1.7}	2.9±0.8 × 10 ⁻¹⁴	7.5±0.8 × 10 ⁻¹⁴	8 – 12	17 ±4	24	2
AP CrB	238.55136	27.36463	199.6 ^{+1.8} _{-2.1}	4.9±1.6 × 10 ⁻¹³	8.7±1.6 × 10 ⁻¹³	8 – 12	24 ±4	22	2
AR Sco	245.44706	-22.88645	116.5 ^{+0.4} _{-0.5}	1.80 × 10 ⁻¹²	...	5.5	7000 ⁺⁵⁰⁰⁰ ₋₂₀₀₀	11	11
V2400 Oph	258.15176	-24.24576	700 ⁺¹⁰ ₋₁₁	4.4±0.4 × 10 ⁻¹¹ *	...	2 – 4	640±120	24	25
V1007 Her	261.02625	41.23535	470 ⁺⁴⁰ ₋₃₀	1.6±0.7 × 10 ⁻¹³	9.4±0.9 × 10 ⁻¹³ *	8 – 12	38 ±9	22	2
V1323 Her	270.91524	40.20558	1830 ⁺¹⁸⁰ ₋₁₄₀	1.6±0.2 × 10 ⁻¹² *	2.0±0.2 × 10 ⁻¹² *	4 – 8	43 ±9	24	2
AM Her	274.05491	49.86811	87.9 ±0.2	1.1±0.1 × 10 ⁻¹⁰ *	...	2 – 4	640 ±120	24	25
...	880±150
V1432 Aql	295.04755	-10.42382	450 ±7.0	2.1 × 10 ⁻¹¹	4.1 × 10 ⁻¹¹	8 – 12	15 ±5	15	2
J1955+0045	298.80199	0.76011	165.5 ^{+1.9} _{-1.5}	1.1±0.1 × 10 ⁻¹¹	1.3±0.1 × 10 ⁻¹¹	8 – 12	79±8*	24	2
AE Aqr	310.03848	-0.87079	91.34 ^{+0.12} _{-0.13}	5.1±0.5 × 10 ⁻¹² *	...	4.9	7500±750*	8	1
HU Aqr	316.99219	-5.29488	189.6 ±1.5	3.3 × 10 ⁻¹⁴	5.4 × 10 ⁻¹⁴	8 – 12	44 ±13	18	2
V388 Peg	329.38469	8.92079	720 ⁺⁸⁰ ₋₅₀	4.1±0.8 × 10 ⁻¹²	6±2 × 10 ⁻¹¹	8 – 12	34 ±5	9	2

Note. — The coordinates and distances in this table were found in Gaia EDR3 and [Bailey-Jones et al. \(2021\)](#) respectively, except for EF Eri, which did not appear in that catalog. That information was taken from [Thorstensen \(2003\)](#). RXJ0502.8+1624 is equivalent to Tau 4 in [Barrett et al. \(2020\)](#). Where there are multiple entries for the same object, the row will begin with a “...” in the “Name” column and anywhere the values are the same as the previous row. Otherwise, a “...” indicates the information is unavailable, such as for our detections and the highlighted objects in Figure 5, since those were not included in Figure 6. In the case of EU UMa, the model from [Ramsay et al. \(2004a\)](#) did not provide enough information to find the flux between 0.1 – 10 keV, so that entry was left blank. Errors on the X-ray and radio flux columns are assumed to be at least 10% and were raised (and marked with an asterisk) if quoted as less in their references. The references in the final two columns are numbered as follows: [1] [Abada-Simon et al. \(1993\)](#), [2] [Barrett et al. \(2020\)](#), [3] [Boller et al. \(2016\)](#), [4] [Bonnet-Bidaud et al. \(2020\)](#), [5] [Collins & Wheatley \(2010\)](#), [6] [Coppejans et al. \(2015\)](#), [7] [Coppejans et al. \(2016\)](#), [8] [Eracleous et al. \(1991\)](#), [9] [Evans et al. \(2020\)](#), [10] [Hewitt et al. \(2020\)](#), [11] [Marsh et al. \(2016\)](#), [12] [Mauche & Mukai \(2002\)](#), [13] [Ramsay et al. \(1994\)](#), [14] [Ramsay et al. \(2004a\)](#), [15] [Rana et al. \(2005\)](#), [16] [Russell et al. \(2016\)](#) [17] [Saitou et al. \(2012\)](#), [18] [Schwarz et al. \(2009\)](#), [19] [Schwope et al. \(2007\)](#), [20] [Still & Mukai \(2001\)](#), [21] [Szkody et al. \(1999\)](#), [22] [Voges et al. \(1999\)](#), [23] [Vogel et al. \(2007\)](#), [24] [Webb et al. \(2020\)](#), [25] this paper.

Gallo E., et al., 2014, *MNRAS*, **445**, 290

Garnavich P., Littlefield C., Kafka S., Kennedy M., Callanan P., Balsara D. S., Lyutikov M., 2019, *ApJ*, **872**, 67

Garnavich P., Littlefield C., Wagner R. M., van Roestel J., Jaodand A. D., Szkody P., Thorstensen J. R., 2021, *ApJ*, **917**, 22

Gawroński M. P., Goździewski K., Katarzyński K., Rycyk G., 2018, *MNRAS*, **475**, 1399

Gordon Y. A., et al., 2020, *Research Notes of the American Astronomical Society*, **4**, 175

Gordon Y. A., et al., 2021, *ApJS*, **255**, 30

Güdel M., 2002, *ARA&A*, **40**, 217

Hallinan G., Antonova A., Doyle J. G., Bourke S., Lane C., Golden A., 2008, *ApJ*, **684**, 644

Henry T. J., et al., 2018, *AJ*, **155**, 265

Hewitt D. M., et al., 2020, *MNRAS*, **496**, 2542

Kennedy M. R., et al., 2020, *MNRAS*, **495**, 4445

King A. R., 1993, *MNRAS*, **261**, 144

Körding E., Rupen M., Knigge C., Fender R., Dhawan V., Templeton M., Muxlow T., 2008, *Science*, **320**, 1318

Lacy M., 2021, VLASS Project Memo 14: Correction of position errors in mosaic images without w-term corrections. NRAO

Lacy M., et al., 2020, *PASP*, **132**, 035001

Langford A., Littlefield C., Garnavich P., Kennedy M. R., Scaringi S., Szkody P., 2022, *AJ*, **163**, 4

Launhardt R., Loinard L., Dzib S. A., Forbrich J., Bower G. C., Henning T. K., Mioduszewski A. J., Reffert S., 2022, *ApJ*, **931**, 43

Ling J., Isella A., Johns-Krull C., Lazio T. J. W., 2022, *ApJ*, **926**, 228

Littlefield C., Scaringi S., Garnavich P., Szkody P., Kennedy M. R., Ilkiewicz

Table 4. The fluxes for non-magnetic CVs used to generate Figure 5 and 6, including QS Vir and SS Cyg. Refer Table 3 for magnetic CVs and the list of citations in the table note.

Name	RA (deg)	Dec (deg)	Distance (pc)	1–10 keV flux (erg s ⁻¹ cm ⁻²)	0.1–10 keV flux (erg s ⁻¹ cm ⁻²)	Radio band (GHz)	Radio flux (μJy)	X-ray ref.	Radio ref.
CM Phe	5.38842	-51.70967	308±3	3.3±0.3×10 ⁻¹² *	4.2±0.4×10 ⁻¹²	0.43 – 2.1	< 30	9	10
RX And	16.14809	41.29928	196.6 ±0.9	7±2 × 10 ⁻¹³	1.0±0.1 × 10 ⁻¹¹ *	8 – 12	19.6 ±4.4	9	7
...	13.6 ±3.2
TT Ari	31.72112	15.29490	247 ±2	2.40 × 10 ⁻¹¹	3.10 × 10 ⁻¹¹	4 – 8	39.6 ±4.2	12	6
...	240 ±24*
IM Eri	66.17152	-20.12003	185.5 ^{+1.0} _{-0.9}	4.3±1.1 × 10 ⁻¹²	5.5±1.0 × 10 ⁻¹²	0.43 – 2.1	99 ±26	3	10
V347 Pup	92.64028	-48.74036	290.3±1.2	1.7±0.4×10 ⁻¹³	2.1±0.6×10 ⁻¹³	0.43 – 2.1	< 30	9	10
U Gem	118.77167	22.00122	93.1 ±0.3	1.0±0.1 × 10 ⁻¹¹ *	1.2±0.1 × 10 ⁻¹¹ *	8 – 12	12.7 ±2.8	24	7
YZ Cnc	122.73616	28.14233	233.5 ^{+1.5} _{-1.8}	8.5±0.8 × 10 ⁻¹² *	1.5±0.2 × 10 ⁻¹¹ *	8 – 12	17.4 ±3.7	24	7
...	26.8 ±5.2
IX Vel	123.82884	-49.22283	90.13±0.14	2.2±0.2×10 ⁻¹² *	4.2±0.4×10 ⁻¹² *	0.43 – 2.1	< 42	24	10
SU Uma	123.11785	62.60612	220.1 ±1.1	5.40 × 10 ⁻¹²	7.60 × 10 ⁻¹²	8 – 12	19.1 ±4.9	5	7
...	58.1 ±5.8*
Z Cam	126.30486	73.11083	213.5 ^{+1.2} _{-1.3}	4.7±0.5 × 10 ⁻¹² *	5.7±0.6 × 10 ⁻¹² *	8 – 12	25.0 ±3.1	17	7
...	40.3 ±5.2
RW Sex	154.98584	-8.69899	221.6 ^{+1.1} _{-1.0}	4.4±0.5 × 10 ⁻¹²	5.6±0.6 × 10 ⁻¹² *	0.86 – 1.7	233 ±36	9	10
...	26.8 ±3.3	...	2
QS Vir	207.46687	-13.22687	50 ^{+0.07} _{-0.06}	8.5±0.9 × 10 ⁻¹³ *	...	2 – 4	970±160	24	25
V1084 Her	250.94041	34.04427	465 ±4	1.6±0.2 × 10 ⁻¹² *	1.8±0.2 × 10 ⁻¹² *	4 – 8	< 10.2 ±3.4	24	6
LS IV -08 3	254.12335	-8.57738	211±2	4.0±0.7×10 ⁻¹²	5.1±0.9×10 ⁻¹²	0.43 – 2.1	< 33	3	10
V341 Ara	254.42249	-63.21105	155.3±0.8	1.2±0.2×10 ⁻¹²	1.5±0.3×10 ⁻¹²	0.43 – 2.1	< 27	9	10
V603 Aql	282.22770	0.58408	315 ⁺³ ₋₄	6.7±1.1 × 10 ⁻¹³	4.3±0.4 × 10 ⁻¹² *	4 – 8	22 ± 3	9	6
...	233 ±36	...	10
V3885 Sgr	296.91905	-42.00751	128.6 ^{+0.6} _{-0.5}	4.8±0.5 × 10 ⁻¹² *	6.1±0.6 × 10 ⁻¹² *	0.43 – 2.1	256 ±26*	9	10
V5662 Sgr	301.46284	-29.58358	169±4	3.3±0.9×10 ⁻¹²	4.2±1.1×10 ⁻¹²	0.43 – 2.1	< 24	3	10
SS Cyg	325.67904	43.58622	112.3 ^{+0.4} _{-0.3}	9.0±0.9 × 10 ⁻¹⁰ *	...	4.6	180 ±20*	16	16
...	4.1 ^{+0.5} _{-0.4} × 10 ⁻¹¹ *	810 ±81*

- K., Mason P. A., 2021, *AJ*, **162**, 49
- Marcote B., Marsh T. R., Stanway E. R., Paragi Z., Blanchard J. M., 2017, *A&A*, **601**, L7
- Marsh T. R., et al., 2016, *Nature*, **537**, 374
- Matranga M., Drake J. J., Kashyap V., Steeghs D., 2012, *ApJ*, **747**, 132
- Mauche C. W., Mukai K., 2002, *ApJ*, **566**, L33
- McMullin J. P., Waters B., Schiebel D., Young W., Golap K., 2007, in Shaw R. A., Hill F., Bell D. J., eds, *Astronomical Society of the Pacific Conference Series Vol. 376, Astronomical Data Analysis Software and Systems XVI*, p. 127
- Meintjes P. J., Venter L. A., 2003, *MNRAS*, **341**, 891
- Mooley K. P., et al., 2017, *MNRAS*, **467**, L31
- O'Donoghue D., Koen C., Kilkenny D., Stobie R. S., Koester D., Bessell M. S., Hambly N., MacGillivray H., 2003, *MNRAS*, **345**, 506
- Owen F. N., Morrison G. E., 2008, *AJ*, **136**, 1889
- Pelisolì I., et al., 2022, *MNRAS*, **509**, L31
- Pretorius M. L., et al., 2021, *MNRAS*, **503**, 3692
- Ramsay G., Mason K. O., Cropper M., Watson M. G., Clayton K. L., 1994, *MNRAS*, **270**, 692
- Ramsay G., Cropper M., Mason K. O., Córdova F. A., Priedhorsky W., 2004a, *MNRAS*, **347**, 95
- Ramsay G., Cropper M., Wu K., Mason K. O., Córdova F. A., Priedhorsky W., 2004b, *MNRAS*, **350**, 1373
- Rana V. R., Singh K. P., Barrett P. E., Buckley D. A. H., 2005, *ApJ*, **625**, 351
- Ritter H., Kolb U., 2003, *A&A*, **404**, 301
- Russell T. D., et al., 2016, *MNRAS*, **460**, 3720
- Saitou K., Tsujimoto M., Ebisawa K., Ishida M., 2012, *PASJ*, **64**, 88
- Schwarz R., Schwöpe A. D., Vogel J., Dhillon V. S., Marsh T. R., Copperwheat C., Littlefair S. P., Kanbach G., 2009, *A&A*, **496**, 833
- Schwöpe A. D., Staude A., Koester D., Vogel J., 2007, *A&A*, **469**, 1027
- Shishkovsky L., et al., 2018, *ApJ*, **855**, 55
- Still M., Mukai K., 2001, *ApJ*, **562**, L71
- Szkody P., Vennes S., Schmidt G. D., Wagner R. M., Fried R., Shafter A. W., Fierce E., 1999, *ApJ*, **520**, 841
- Takata J., Hu C. P., Lin L. C. C., Tam P. H. T., Pal P. S., Hui C. Y., Kong A. K. H., Cheng K. S., 2018, *ApJ*, **853**, 106
- Taylor M. B., 2005, in Shopbell P., Britton M., Ebert R., eds, *Astronomical Society of the Pacific Conference Series Vol. 347, Astronomical Data Analysis Software and Systems XIV*, p. 29
- Thorstensen J. R., 2003, *AJ*, **126**, 3017
- Thorstensen J. R., 2020, *AJ*, **160**, 151
- Tudor V., et al., 2017, *MNRAS*, **470**, 324
- Vogel J., Schwöpe A. D., Gänsicke B. T., 2007, *A&A*, **464**, 647
- Voges W., et al., 1999, *A&A*, **349**, 389
- Warner B., 2003, *Cataclysmic Variable Stars*, doi:10.1017/CBO9780511586491.
- Webb N. A., et al., 2020, *A&A*, **641**, A136
- Wynn G. A., King A. R., Horne K., 1997, *MNRAS*, **286**, 436
- Zhao Y., et al., 2020, *MNRAS*, **493**, 6033

This paper has been typeset from a \LaTeX file prepared by the author.